Digital Object Identifier 10.1109/TIA.2023.3296388

IEEE Transactions on Industry Applications

Modeling of Asymmetrical Grid Faults for P-HIL Accuracy and Stability Analysis in LVRT Tests

Sante Pugliese
Marco Liserre
Muhammad Usman Rafiq

Suggested Citation

S. Pugliese, M. Liserre and M. U. Rafiq, "Modeling of Asymmetrical Grid Faults for P-HIL Accuracy and Stability Analysis in LVRT Tests," in IEEE Transactions on Industry Applications, vol. 59, no. 6, pp. 6926-6940, Nov.-Dec. 2023

Modeling of Asymmetrical Grid Faults for P-HIL Accuracy and Stability Analysis in LVRT Tests

Sante Pugliese, *Member, IEEE,* Marco Liserre, *Fellow, IEEE*, and Muhammad Usman Rafiq

***Abstract*—The energy systems are evolving towards a comprehensive and massive integration of power electronic based technologies such as photovoltaics, wind turbines and electric vehicles. All of these emerging and promising power conversion technologies need to be tested for grid codes compliance, especially during severe grid fault events, before their commercialisation. Low-voltage ride-through (LVRT) field tests are conducted to prove the ability of the converter to ride through faults. These field tests are expensive and require bulky equipment, whereas power-hardware-in-the-loop (P-HIL) offers a more cost-effective and flexible alternative. However, the P-HIL must be stable and accurate to provide reliable results. The accuracy of a P-HIL test is directly influenced by its interface algorithm. This paper proposes a frequency domain approach, based on the concept of singular values in multi-input multi-output (MIMO) systems, to study the P-HIL accuracy and stability in grid-connected converter testing under asymmetrical line-to-line fault conditions. The accuracy and stability analysis was performed analytically and validated by Matlab/Simulink simulations and by experimental P-HIL tests. This paper demonstrates that correct fault modeling leads to correct assessment of the reactive power injected under faults and resonances avoidance.**

***Index Terms*—Power-hardware-in-the-loop, real-time simulation, P-HIL accuracy, MIMO systems, stability criteria, LVRT.**

I. Introduction

A More reliable connection of the high share of renewable energy to the electrical power system can be achieved if the grid converters are equipped with low-voltage ride-through (LVRT) capability. Early generation of inverters did not provide any support mechanism to the grid. They would feed active power into the system during normal operation and disconnect in the event of a fault. As a result, grid operators have defined specific rules and requirements, in the form of grid codes [1], [2] against which inverters need to be tested prior to their commercialisation, especially during severe grid fault events. For example, they must support the grid by injecting reactive power during voltage dips and ride through faults (LVRT capability). LVRT tests are usually carried out in the field, where a fault-ride-through (FRT) container, based on the principle of a passive voltage divider, is connected between the point of common coupling (PCC) of the converter and the medium-voltage power grid, to emulate various voltage dips at the PCC of the device under test (DUT) [3], [4]. In addition, according to the German FGW TR3 guidelines, the grid short-circuit power should be at least three times the nominal apparent power of the DUT and an X/R ratio of at least three is required at the PCC of the DUT [3]. However, LVRT tests performed with passive voltage dividers are expensive, time-consuming, and they require a bulky and inflexible system developed on purpose only for such tests.

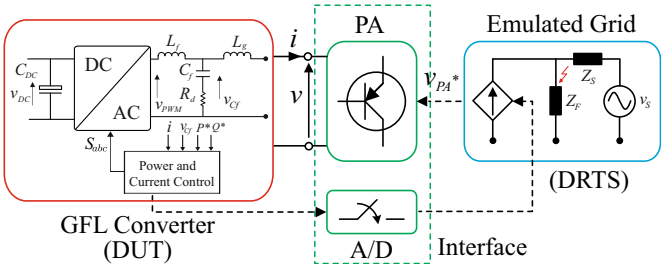

Fig. 1. P-HIL scheme for GFL converters testing under grid fault conditions.

Instead, Power-hardware-in-the-loop (P-HIL) is a flexible and effective method to test a power converter under different realistic grid conditions and scenarios [5]–[8]. A generic P-HIL consists of a digital real-time simulator (DRTS), a power amplifier (PA) and a DUT, where the PA is the power interface between the DUT and the real-time simulation, as shown in Fig. 1. These elements are connected together via an interface algorithm (IA), which is critical for the stability of the P-HIL test and the accuracy of the results [9]–[12]. Therefore, the failure scenario can be simulated in the DRTS and the DUT behaviour can be studied and analysed in real-time.

Despite several studies on P-HIL for reconfigurable real-time grid emulators in power systems with high penetration of renewable and broadband frequency grid impedance have been published in literature [13]–[18], only few of them use and analyse the P-HIL as a tool for testing the fault behaviour of power converters in distribution networks [16]–[18]. In all these works, particular attention has been paid to the accuracy and the stability analysis of the P-HIL under symmetrical grid faults [16], [17], while only a few results on P-HIL based LVRT tests of power converters under asymmetrical grid faults are presented in [18]. Here it is concluded that asymmetrical voltage dips in the grid are not accurately generated, regardless of whether the grid emulator is in open-loop or closed-loop control. The reason for this is that the control system bandwidth is not wide enough to execute negative sequence

This paper was supported by Interreg Deutschland-Danmark with funds from the European Regional Development Fund via the PE-Region Platform project (ref. 098-1.1-18) and the Smart Power Conversion project (ref.16-2,1-221). *(Corresponding author: Sante Pugliese.)*

S. Pugliese and M. Liserre are with the Chair of Power Electronics, Kiel University, Kiel, 24143, Germany (e-mail: sapu@tf.uni-kiel.de, ml@tf.uni-kiel.de). M. U. Rafiq is with Maschinenfabrik Reinhausen GmbH, Erfurt, 99092, Germany (e-mail: m.rafiq@reinhausen.com).

components without gain and phase errors. However, these conclusions were not supported by a systematic accuracy analysis based on a mathematical model of the P-HIL under asymmetrical faults.

In [19], the behaviour of grid-following (GFL) converters under symmetrical and asymmetrical faults in P-HIL tests is systematically investigated for the first time. An analytical definition of accuracy based on the equivalent impedance model of the fault is given, with particular emphasis on the effects of the interface algorithm on the severity of the grid fault. The accuracy analysis of the P-HIL has been carried out in the frequency domain by using Bode diagrams for symmetrical faults, which behave like single-input single-output (SISO) systems. Furthermore, an innovative approach based on the definition of singular values has been proposed to study the P-HIL accuracy for line-to-line asymmetrical faults, which are modelled as multi-input multi-output (MIMO) systems. In both the cases, the ideal transformer method (ITM) has been used as the interface algorithm. A comparison between the results of the naturally coupled system (NCS) and the P-HIL is performed, both in simulation and in laboratory, to prove the correctness of the proposed model and the P-HIL accuracy analysis.

In this paper, the models derived in [19] are used to study the stability of P-HIL under fault scenarios, which is the added contribution to our previous work. In fact, the proposed fault modeling provides the grid impedance in the form of a matrix, which is used in the stability analysis of P-HIL setups by means of the generalized Nyquist criterion (GNC) for MIMO systems [20]. Additionally, with the support of the stability analysis, it is possible to properly design the bandwidth of the low-pass filter (LPF) required to stabilise the ITM, as a trade-off between robust stability and accuracy of the P-HIL system. The rest of the paper is structured as follows: in Section II, the definition of accuracy in P-HIL is given, while in Section III, the modeling and the P-HIL accuracy analysis in line-to-line asymmetrical fault by using the concept of singular values and directions in MIMO systems are presented. Section IV presents the P-HIL stability analysis of a GFL converter connected to a line-to-line faulty grid. In Section V, the analytical findings of the P-HIL accuracy and stability of the previous sections are experimentally validated. Finally, Section VI concludes the paper.

II. Definition of Accuracy in P-HIL

An equivalent impedance-based representation of a P-HIL system for GFL converter testing can be derived as shown in Fig. 2. Here, Z_{PHIL} represents the emulated real-time grid impedance, defined as the transfer function between voltage and current at the PCC, which includes the model of the simulated grid, the interface algorithm, and the power amplifier contributions. Furthermore, Z_{PHIL} is represented as a variable impedance since it can change during normal or fault operation (time-varying behaviour) and its model depends on the selected P-HIL interface algorithm. The DUT is modelled as a current source with a parallel impedance Z_{GFL}.

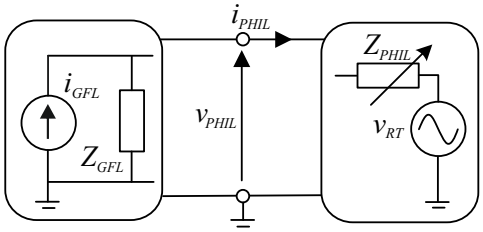

Fig. 2. Equivalent impedance model of a P-HIL setup for GFL converter testing.

The accuracy of a P-HIL setup in power electronics and power system applications can be defined in terms of an error transfer function calculated as the ratio between the emulated impedance Z_{PHIL}, and the ideal impedance of the plant, Z_{NCS}.

$$Z_{error}(j\omega) = \left(\frac{|Z_{PHIL}(j\omega)|}{|Z_{NCS}(j\omega)|}\right)_{dB} \cdot \frac{e^{\angle(Z_{PHIL}(j\omega))}}{e^{\angle(Z_{NCS}(j\omega))}} \quad (1)$$

An ideal P-HIL generates an equivalent impedance model that behaves like the naturally coupled system all over the relevant frequency range [12].

III. Modeling and P-HIL Accuracy Analysis in Asymmetrical Grid Faults

This section presents the modeling and accuracy analysis of a line-to-line asymmetrical grid fault both in NCS and in a P-HIL system based on the ITM interface algorithm. The choice of a line-to-line fault is made to limit the analysis only to the modeling of the positive and negative sequence voltages experienced by a grid-connected converter, when an asymmetrical grid fault occurs. In fact, a line-to-line grid fault does not generate zero-sequence voltages [21]. Furthermore, in a power system under fault condition, the type of sag experienced by a system connected to a given ac-bus does not only depend on the number of phases affected by the grid fault, but it is also influenced by the transformers located between the ac-bus and the fault point. In grid-connected applications, an isolating three-phase transformer is usually connected at the PCC of the converter. As a result, the amplitude and phase of the unbalanced voltages resulting from a given fault are modified into a new type of fault when propagating through three-phase transformers. Moreover, the zero-sequence component present in line-to-ground faults does not propagate from the grid-side to the converter-side of the transformer. For these reasons, and without loss of generality, a line-to-line fault is considered in this paper. However, similar modeling and P-HIL accuracy results can be obtained by considering other types of faults, such as symmetrical faults in [19].

A. Line-to-Line Asymmetrical Grid Fault Modeling

An overview of the system under investigation is given in Fig. 3. It shows the three-phase circuit of an asymmetrical line-to-line grid fault, where a GFL converter (i.e. the DUT), modelled with ideal current sources, is connected to the PCC and injects positive and negative sequence currents in each

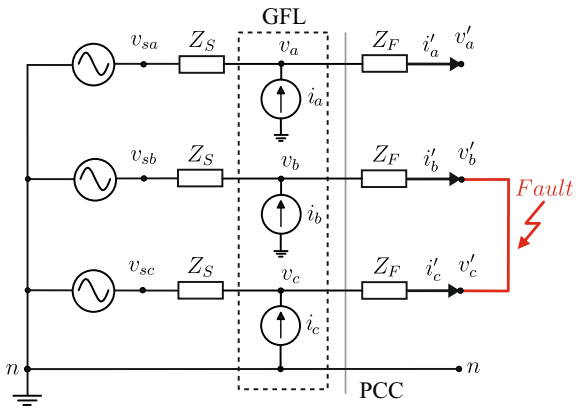

Fig. 3. Three-phase circuit of a line-to-line grid fault between phase-b and phase-c.

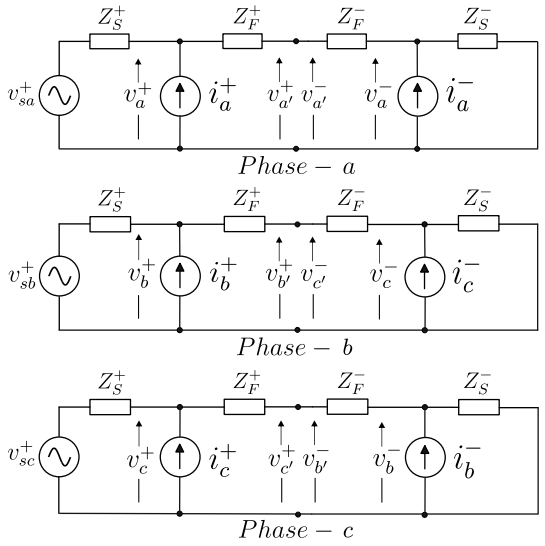

Fig. 4. Positive and negative sequence components based circuit of a GFL converter connected at the PCC of a line-to-line asymmetrical grid fault.

phase. The power grid is modelled with a symmetrical and positive voltage (v_s). In the line-to-line grid fault under investigation, phase-b and phase-c are short-circuited, so the voltage at the fault point v'_b is equal to v'_c, ($v'_b = v'_c$). The currents at the fault point satisfy the following conditions: for phase-b and phase-c, they are equal and opposite, $i'_b = -i'_c$, while for phase-a, $i'_a = 0$. Given these conditions, the equivalent model at the sequence components of the line-to-line fault can be derived. The positive, the negative and the zero-sequence voltages ($v^+_{a'}$, $v^-_{a'}$, $v^o_{a'}$) and currents ($i^+_{a'}$, $i^-_{a'}$, $i^o_{a'}$) at the fault point are calculated with the *Fortescue* transformation as:

$$\begin{bmatrix} v^+_{a'} \\ v^-_{a'} \\ v^o_{a'} \end{bmatrix} = \frac{1}{3}\begin{bmatrix} 1 & \alpha & \alpha^2 \\ 1 & \alpha^2 & \alpha \\ 1 & 1 & 1 \end{bmatrix}\begin{bmatrix} v'_a \\ v'_b \\ v'_c \end{bmatrix} = \frac{1}{3}\begin{bmatrix} v'_a - v'_b \\ v'_a - v'_b \\ v'_a + 2v'_b \end{bmatrix} \tag{2}$$

$$\begin{bmatrix} i^+_{a'} \\ i^-_{a'} \\ i^o_{a'} \end{bmatrix} = \frac{1}{3}\begin{bmatrix} 1 & \alpha & \alpha^2 \\ 1 & \alpha^2 & \alpha \\ 1 & 1 & 1 \end{bmatrix}\begin{bmatrix} i'_a \\ i'_b \\ i'_c \end{bmatrix} = \frac{1}{\sqrt{3}}\begin{bmatrix} j(i'_b) \\ -j(i'_b) \\ 0 \end{bmatrix} \tag{3}$$

where $\alpha = e^{j\frac{2\pi}{3}}$ is the *Fortescue* operator. The voltage phasors in (2) indicate that the positive and negative sequence voltage components are equal at the fault point, $v^+_{a'} = v^-_{a'}$. Likewise, the current phasors in (3) indicate that the zero-sequence component of the line currents is zero in a line-to-line fault, while the positive and negative sequence currents satisfy the condition $i^+_{a'} = -i^-_{a'}$.

Figure 4 shows, for each phase, the equivalent positive and negative sequence-based circuit of a GFL converter connected at the PCC of a line-to-line grid fault. The zero-sequence model is neglected as it does not contribute to the PCC voltage, $v^o_a = 0$. Assuming that the positive and negative sequence line impedances at the source side are equal, (i.e. $Z^+_S = Z^-_S = Z_S$) and that the GFL current contribution is zero, the circuit in Fig. 4 results in the following voltages at the PCC for phase-a:

$$\begin{aligned} v^+_a &= \frac{Z_S + (Z^+_F + Z^-_F)}{2Z_S + (Z^+_F + Z^-_F)} v^+_{sa} \\ v^-_a &= \frac{Z_S}{2Z_S + (Z^+_F + Z^-_F)} v^+_{sa}. \end{aligned} \tag{4}$$

The severity of the grid fault observed at the PCC can be assessed by means of the dip parameter $\vec{D}$, which is defined as follows:

$$\vec{D} = \frac{(Z^+_F + Z^-_F)}{2Z_S + (Z^+_F + Z^-_F)}. \tag{5}$$

The dip parameter $\vec{D} = D\angle\rho_D$ defines the relationship between the line impedance at the fault side Z_F and the source side Z_S. Its magnitude depends on the distance between the PCC and the fault point, while its phase depends on the X/R ratio on both sides of the PCC. The positive and negative sequence voltages at the PCC of phase-a in (4) can be written as a function of $\vec{D}$:

$$\begin{bmatrix} v^+_a \\ v^-_a \end{bmatrix} = \frac{1}{2}\begin{bmatrix} 1+\vec{D} \\ 1-\vec{D} \end{bmatrix} v^+_{sa} = \begin{bmatrix} \vec{D}^+ \\ \vec{D}^- \end{bmatrix} v^+_{sa} \tag{6}$$

with:

$$\vec{D}^+ = \frac{1}{2}(1+\vec{D}), \quad \vec{D}^- = \frac{1}{2}(1-\vec{D}). \tag{7}$$

The products $\vec{D}^+ v^+_{sa}$ and $\vec{D}^- v^+_{sa}$ in (6) are known as the 'characteristic voltage' of the voltage sag, for the positive and negative sequences respectively [21]. Applying the superposition theorem to the sequences circuit in Fig. 4, the sequence voltages at the PCC for phase-a can be written as a function of the source voltage v^+_{sa}, the positive and negative sequence currents (i^+_a and i^-_a) of the GFL converter as follows:

$$\begin{aligned} v^+_a &= \vec{D}^+ v^+_{sa} + Z^+_{NCS} i^+_a + Z^-_{NCS} i^-_a \\ v^-_a &= \vec{D}^- v^+_{sa} + Z^-_{NCS} i^+_a + Z^+_{NCS} i^-_a \end{aligned} \tag{8}$$

where:

$$Z^+_{NCS} = \vec{D}^+ Z_S, \quad Z^-_{NCS} = \vec{D}^- Z_S. \tag{9}$$

With $v^+_{a'} = v^-_{a'}$, the sequence components for phase-b and phase-c at the fault point are given by

$$\begin{aligned} v^+_{b'} = \alpha^2 v^+_{a'}, \quad v^-_{c'} = \alpha^2 v^-_{a'} &\implies v^+_{b'} = v^-_{c'} \\ v^+_{c'} = \alpha v^+_{a'}, \quad v^-_{b'} = \alpha v^-_{a'} &\implies v^+_{c'} = v^-_{b'}. \end{aligned} \tag{10}$$

The equivalent sequence-based representation of phase-b and phase-c is shown in Fig. 4, while in (11) and (12) are given the PCC sequence voltages associated with the voltage sources of phase-b and phase-c respectively. Due to the short-circuit, the contributions of i_c^- and i_b^- can be seen on the positive sequence of phase-b and phase-c, respectively.

$$\begin{aligned} v_b^+ &= \vec{D}^+ v_{sb}^+ + Z_{NCS}^+ i_b^+ + Z_{NCS}^- i_c^- \\ v_c^- &= \vec{D}^- v_{sb}^+ + Z_{NCS}^- i_b^+ + Z_{NCS}^+ i_c^- \end{aligned} \tag{11}$$

$$\begin{aligned} v_c^+ &= \vec{D}^+ v_{sc}^+ + Z_{NCS}^+ i_c^+ + Z_{NCS}^- i_b^- \\ v_b^- &= \vec{D}^- v_{sc}^+ + Z_{NCS}^- i_c^+ + Z_{NCS}^+ i_b^- \end{aligned} \tag{12}$$

The former equations (8), (11) and (12) can be rearranged in terms of positive and negative sequence vectors in the stationary abc-reference frame as follows,

$$\underbrace{\begin{bmatrix} v_a^+ \\ v_b^+ \\ v_c^+ \end{bmatrix}}_{\boldsymbol{v}^+} = \vec{D}^+ \underbrace{\begin{bmatrix} v_{sa}^+ \\ v_{sb}^+ \\ v_{sc}^+ \end{bmatrix}}_{\boldsymbol{v_s^+}} + Z_{NCS}^+ \underbrace{\begin{bmatrix} i_a^+ \\ i_b^+ \\ i_c^+ \end{bmatrix}}_{\boldsymbol{i}^+} + Z_{NCS}^- \underbrace{\begin{bmatrix} i_a^- \\ i_c^- \\ i_b^- \end{bmatrix}}_{\boldsymbol{i}^-} \tag{13}$$

$$\underbrace{\begin{bmatrix} v_a^- \\ v_c^- \\ v_b^- \end{bmatrix}}_{\boldsymbol{v}^-} = \vec{D}^- \underbrace{\begin{bmatrix} v_{sa}^+ \\ v_{sb}^+ \\ v_{sc}^+ \end{bmatrix}}_{\boldsymbol{v_s^+}} + Z_{NCS}^- \underbrace{\begin{bmatrix} i_a^+ \\ i_b^+ \\ i_c^+ \end{bmatrix}}_{\boldsymbol{i}^+} + Z_{NCS}^+ \underbrace{\begin{bmatrix} i_a^- \\ i_c^- \\ i_b^- \end{bmatrix}}_{\boldsymbol{i}^-} \tag{14}$$

and in a more compact notation, (13) and (14) result in:

$$\begin{bmatrix} \boldsymbol{v}^+ \\ \boldsymbol{v}^- \end{bmatrix} = \begin{bmatrix} \vec{D}^+ \\ \vec{D}^- \end{bmatrix} \boldsymbol{v_s^+} + \begin{bmatrix} Z_{NCS}^+ & Z_{NCS}^- \\ Z_{NCS}^- & Z_{NCS}^+ \end{bmatrix} \begin{bmatrix} \boldsymbol{i}^+ \\ \boldsymbol{i}^- \end{bmatrix} \tag{15}$$

Equation (15) represents the equivalent Thevenin MIMO model of a line-to-line grid fault as it appears at the PCC of a GFL converter. The fault impedance of the NCS is defined in terms of a (2x2) transfer matrix by considering the positive and negative sequence current contributions. In (15), $\boldsymbol{i}^+$ and $\boldsymbol{i}^-$ are rotating vectors in the $\Re - \Im$ complex plane and they represent for the positive and negative sequence components of the input current (e.g. GFL current) vector, respectively. While, $\boldsymbol{v}^+$ and $\boldsymbol{v}^-$ are the positive and negative sequence components of the output voltage (e.g. PCC voltage) vector, respectively.

B. Modeling of Line-to-Line Grid Faults in P-HIL

This section provides the equivalent P-HIL representation of a line-to-line grid fault, like the one in Fig. 3, when it is simulated in a DRTS. The ITM interface algorithm has been used to close the P-HIL. Figure 5 shows an equivalent sequence-based representation of phase-a in the ITM-based P-HIL. The positive and negative sequence hardware currents of the GFL converter are measured and fed into the DRTS. Here the currents are sampled with a time step of T_{RT} = 50 μs, filtered with a stabilising first-order LPF,

$$G_{LPF} = \frac{\omega_c}{s + \omega_c} \tag{16}$$

and fed into the positive and negative equivalent sub-circuit model of the PCC via an ideal current source. At the same time, the PCC positive and negative sequence voltages sensed on the DRTS side are sent to the PA, closing the loop. The

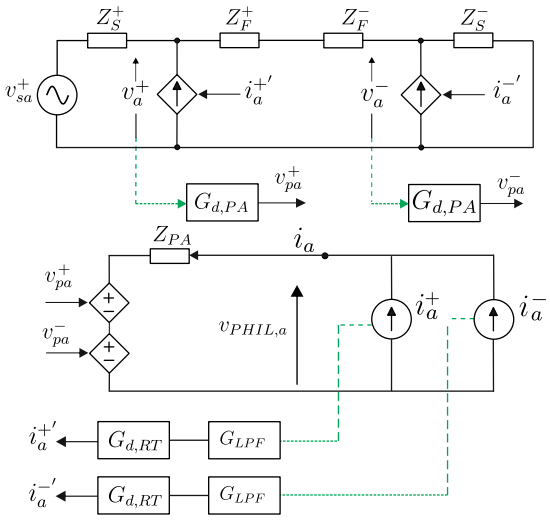

Fig. 5. Sequence-based representation of the not-faulty phase (phase-a) in a line-to-line grid fault with ITM-based P-HIL.

LPF bandwidth, ω_c, is chosen as a trade-off between accuracy and stability of the P-HIL, since the lower the bandwidth, the less accurate the system [11]. Its design is presented in detail in Section IV-C.

$G_{d,RT}$ and $G_{d,PA}$ are the delays due to the DRTS sampling and the PA respectively. Each delay is represented by an equivalent first-order Padé approximation transfer function as $G_{d,x}(s)$:

$$G_{d,x}(s) = \frac{2 - T_x s}{2 + T_x s} \tag{17}$$

where T_x is a generic x time delay, and it can assume the specific value of the DRTS delay (T_{RT}), or the PA delay (T_{PA}). In Fig. 5, Z_{PA} is the impedance of an ac-filter used at the coupling point between the DUT and the PA, and it is expressed as:

$$Z_{PA}(s) = L_{pa} s + R_{pa} \tag{18}$$

where L_{pa} and R_{pa} are the inductive and resistive part of the ac-filter, respectively. The positive and negative sequence voltages of phase-a at the PCC, on the hardware side, are derived as follows:

$$\begin{aligned} v_{PHIL,a}^+ &= G_{d,PA} \vec{D}^+ v_{sa}^+ + Z_{PHIL}^+ i_a^+ + Z_{PHIL}^- i_a^- \\ v_{PHIL,a}^- &= G_{d,PA} \vec{D}^- v_{sa}^+ + Z_{PHIL}^- i_a^+ + Z_{PHIL}^+ i_a^- \end{aligned} \tag{19}$$

where:

$$\begin{aligned} Z_{PHIL}^+ &= G_{LPF} G_{d,RT} G_{d,PA} \vec{D}^+ Z_S + Z_{PA} \\ Z_{PHIL}^- &= G_{LPF} G_{d,RT} G_{d,PA} \vec{D}^- Z_S. \end{aligned} \tag{20}$$

Figure 6 shows the sequence representation of the faulty phases (phase-b and phase-c) in the ITM-based P-HIL. In this case, the positive and negative PCC currents of phase-b and phase-c are fed into the current sources of the DRTS accordingly. Similarly, the PCC voltage equations for phase-b and phase-c of the main power supply are derived in (21) and (22) respectively.

$$\begin{aligned} v_{PHIL,b}^+ &= G_{d,PA} \vec{D}^+ v_{sb}^+ + Z_{PHIL}^+ i_b^+ + Z_{PHIL}^- i_c^- \\ v_{PHIL,c}^- &= G_{d,PA} \vec{D}^- v_{sb}^+ + Z_{PHIL}^- i_b^+ + Z_{PHIL}^+ i_c^- \end{aligned} \tag{21}$$

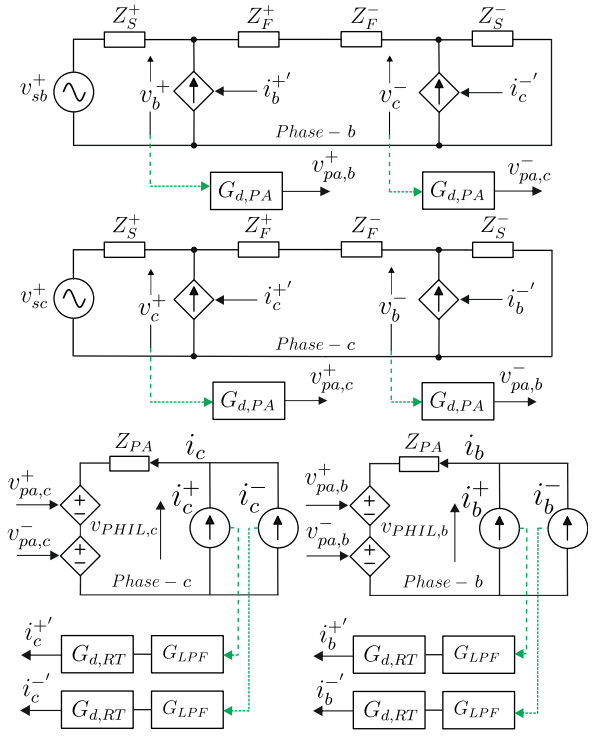

Fig. 6. Sequence-based representation of the faulty phases (phase-b and phase-c) in a line-to-line grid fault with ITM-based P-HIL.

$$\begin{aligned} v_{PHIL,c}^+ &= G_{d,PA}\vec{D}^+ v_{sc}^+ + Z_{PHIL}^+ i_c^+ + Z_{PHIL}^- i_b^- \\ v_{PHIL,b}^- &= G_{d,PA}\vec{D}^- v_{sc}^+ + Z_{PHIL}^- i_c^+ + Z_{PHIL}^+ i_b^- \end{aligned} \tag{22}$$

The previous equations for the PCC voltages of the P-HIL, (19), (21) and (22) can be rearranged in terms of positive and negative sequence vectors in the stationary abc-reference frame as follows

$$\underbrace{\begin{bmatrix} v_{P,a}^+ \\ v_{P,b}^+ \\ v_{P,c}^+ \end{bmatrix}}_{\boldsymbol{v_{PHIL}^+}} = G_{d,PA}\vec{D}^+ \underbrace{\begin{bmatrix} v_{sa}^+ \\ v_{sb}^+ \\ v_{sc}^+ \end{bmatrix}}_{\boldsymbol{v_s^+}} + Z_{PHIL}^+ \underbrace{\begin{bmatrix} i_a^+ \\ i_b^+ \\ i_c^+ \end{bmatrix}}_{\boldsymbol{i^+}} + Z_{PHIL}^- \underbrace{\begin{bmatrix} i_a^- \\ i_c^- \\ i_b^- \end{bmatrix}}_{\boldsymbol{i^-}} \tag{23}$$

$$\underbrace{\begin{bmatrix} v_{P,a}^- \\ v_{P,c}^- \\ v_{P,b}^- \end{bmatrix}}_{\boldsymbol{v_{PHIL}^-}} = G_{d,PA}\vec{D}^- \underbrace{\begin{bmatrix} v_{sa}^+ \\ v_{sb}^+ \\ v_{sc}^+ \end{bmatrix}}_{\boldsymbol{v_s^+}} + Z_{PHIL}^- \underbrace{\begin{bmatrix} i_a^+ \\ i_b^+ \\ i_c^+ \end{bmatrix}}_{\boldsymbol{i^+}} + Z_{PHIL}^+ \underbrace{\begin{bmatrix} i_a^- \\ i_c^- \\ i_b^- \end{bmatrix}}_{\boldsymbol{i^-}} \tag{24}$$

and in a more compact notation, (23) and (24) result in:

$$\begin{bmatrix} \boldsymbol{v_{PHIL}^+} \\ \boldsymbol{v_{PHIL}^-} \end{bmatrix} = G_{d,PA} \begin{bmatrix} \vec{D}^+ \\ \vec{D}^- \end{bmatrix} \boldsymbol{v_s^+} + \begin{bmatrix} Z_{PHIL}^+ & Z_{PHIL}^- \\ Z_{PHIL}^- & Z_{PHIL}^+ \end{bmatrix} \begin{bmatrix} \boldsymbol{i^+} \\ \boldsymbol{i^-} \end{bmatrix} \tag{25}$$

Equation (25) represents the equivalent Thevenin MIMO model of a line-to-line grid fault as it appears at the PCC of a GFL converter in an ITM-based P-HIL.

C. Accuracy Analysis of Line-to-Line Grid Faults in P-HIL

In case of asymmetrical faults, the converter should inject both positive and negative sequence currents into the faulted PCC [1]–[3]. In (25), the positive and negative voltage sag characteristics $\vec{D}^{\pm} v_s^+$ are multiplied by the PA delay transfer function, $G_{d,PA}$. However, it can be assumed that $G_{d,PA}\vec{D}^{\pm} v_s^+ \approx \vec{D}^{\pm} v_s^+$ since the contribution of $G_{d,PA}$ in the magnitude and phase is negligible at low frequencies (i.e. at the fundamental frequency). With this assumption, the accuracy can be studied by comparing the equivalent fault impedance of both the NCS and the P-HIL. These are defined as a (2x2) MIMO system when taking into account their positive and negative sequence contribution.

$$\begin{bmatrix} \boldsymbol{v}^+ \\ \boldsymbol{v}^- \end{bmatrix} = \underbrace{\begin{bmatrix} Z^+ & Z^- \\ Z^- & Z^+ \end{bmatrix}}_{\mathbf{Z}} \begin{bmatrix} \boldsymbol{i}^+ \\ \boldsymbol{i}^- \end{bmatrix} \tag{26}$$

$\mathbf{Z}$ is equal to $\mathbf{Z_N}$ in the NCS, and equal to $\mathbf{Z_P}$ in the P-HIL.

$$\mathbf{Z_N} = \begin{bmatrix} Z_{NCS}^+ & Z_{NCS}^- \\ Z_{NCS}^- & Z_{NCS}^+ \end{bmatrix}, \ \mathbf{Z_P} = \begin{bmatrix} Z_{PHIL}^+ & Z_{PHIL}^- \\ Z_{PHIL}^- & Z_{PHIL}^+ \end{bmatrix} \tag{27}$$

In P-HIL accuracy analysis, it is important to derive the dynamic response of the system in the frequency domain. P-HIL in asymmetrical faults has a MIMO nature, and defining the gain of the system at given frequencies is not a simple task in such systems where the input and output signals are both vectors. A MIMO system has additional degrees of freedom and the system gain also depends on the direction of the input vector. In general, the magnitudes of the eigenvalues of a transfer function matrix, e.g. $|\lambda_i(\mathbf{Z}(j\omega))|$, do not provide a useful means of generalising the SISO gain, $|\mathbf{Z}(j\omega)|$. Eigenvalues are a poor measure of gain, because they measure the gain for the special case when the inputs and the outputs are in the same direction, namely in the direction of the eigenvectors [22]. Eigenvalues can be useful for stability analysis, but not for performance analysis, such as frequency-domain error functions which are used to evaluate the effectiveness of a feedback control. Instead, the singular values are suitable for evaluating the dynamic response of MIMO systems in the frequency domain and are used in this paper to study the P-HIL accuracy under asymmetrical grid fault conditions.

Singular Values Definition: the singular values of a rank-r matrix $\mathbf{A} \in \mathbb{C}^{(mxn)}$, and denoted as $\sigma_i(\mathbf{A})$, are the non-negative square roots of the eigenvalues of $\mathbf{A}^T\mathbf{A}$ ordered such that $\sigma_1 \geq \sigma_2 \geq ... \geq \sigma_p > 0$, $p = min\{m, n\}$.

$$\sigma_i(\mathbf{A}) = \sqrt{\lambda_i(\mathbf{A}^T\mathbf{A})} \tag{28}$$

If $r < p$ then there are $(p - r)$ zero singular values, i.e., $\sigma_{r+1} = \sigma_{r+2} = ... = \sigma_p = 0$. The greatest singular value σ_1 is denoted as $\overline{\sigma}(\mathbf{A}) \triangleq \sigma_1$. When $\mathbf{A}$ is a square (nxn) matrix, then the n-th singular value (i.e., the least singular value) is denoted as $\underline{\sigma}(\mathbf{A}) \triangleq \sigma_n$.

Singular value decomposition (SVD): is a valuable concept for understanding the MIMO system in the frequency domain. SVD states that any matrix $\mathbf{A}_{(m\times n)}$ can be decomposed into an output rotation $\mathbf{U}_{(m\times m)}$, a scaling $\sum_{(m\times n)}$, and an input rotation matrix $\mathbf{W}^T_{(n\times n)}$. The diagonal entries of $\sum$ are the rank-r non-negative and not-zero singular values of the system, $\sigma_i(\mathbf{A})$, arranged in descending order along its main diagonal, while the other entries are zero.

$$\mathbf{A}_{(m\times n)} = \mathbf{U}_{(m\times m)} \sum_{(m\times n)} \mathbf{W}^T_{(n\times n)} \tag{29}$$

$$\sum_{(m\times n)} = \begin{bmatrix} \sigma_1 & 0 & 0 & \dots & 0 & \dots & 0 \\ 0 & \sigma_2 & 0 & \dots & 0 & \dots & 0 \\ \vdots & & \sigma_i & & & & \vdots \\ & & & \ddots & & & \\ 0 & & & & \sigma_r & \dots & 0 \\ & \dots & & & & & \\ 0 & & & & 0 & \dots & 0 \end{bmatrix} \tag{30}$$

SVD Symmetry Corollary: if $\mathbf{A}$ is a symmetric matrix the singular values are the absolute values of the eigenvalues of $\mathbf{A}$: $\sigma_i(\mathbf{A}) = |\lambda_i(\mathbf{A})|$.

Input and output directions: The column vectors of $\mathbf{U}$, denoted as u_i, represent the output directions of the system and they are orthogonal $u_i^T u_i = 1$, $u_i^T u_j = 0$, $i \neq j$ and orthonormal (unit length) each others. Similarly, the column vectors of $\mathbf{W}$, denoted as w_i, represent the input directions of the system, and they are orthogonal and orthonormal each others. These input and output directions are related through the singular values and in particular, the vector $\overline{w} = w_1$ corresponds to the input direction with the largest amplification $\overline{\sigma}(\mathbf{A})$, while the vector $\underline{w} = w_p$ corresponds to the input direction with the smallest amplification $\underline{\sigma}(\mathbf{A})$:

$$\overline{\sigma}(\mathbf{A}) = \frac{\|\mathbf{A}\overline{w}\|_2}{\|\overline{w}\|_2}, \quad \underline{\sigma}(\mathbf{A}) = \frac{\|\mathbf{A}\underline{w}\|_2}{\|\underline{w}\|_2}. \tag{31}$$

The system under investigation, namely $\mathbf{Z}(j\omega)$ in (26), is a (2x2) symmetric transfer matrix with two different singular values. For each angular frequency ω, these singular values represent the maximum and minimum gain of the system as the input current vector $\boldsymbol{i} = [\boldsymbol{i}^+ \quad \boldsymbol{i}^-]^T$ varies in all possible directions. Since $\mathbf{Z}(j\omega)$ is a symmetric matrix, the SVD symmetry corollary holds and the singular values can be derived from the eigenvalues as follows:

$$\begin{aligned} \overline{\sigma}(\omega) &= max\{|\lambda_1(j\omega)|, |\lambda_2(j\omega)|\} \\ \underline{\sigma}(\omega) &= min\{|\lambda_1(j\omega)|, |\lambda_2(j\omega)|\} \end{aligned} \tag{32}$$

where:

$$\begin{aligned} \lambda_1(j\omega) &= \lambda_1(\mathbf{Z}(j\omega)) = Z^+(j\omega) + Z^-(j\omega) \\ \lambda_2(j\omega) &= \lambda_2(\mathbf{Z}(j\omega)) = Z^+(j\omega) - Z^-(j\omega). \end{aligned} \tag{33}$$

$\lambda_1(j\omega)$ and $\lambda_2(j\omega)$ are the eigenvalues of $\mathbf{Z}(j\omega)$ calculated at ω in closed form as $det[\lambda\mathbf{I} - \mathbf{Z}(j\omega)] = 0$. The input directions associated with each singular value can be obtained from the SVD applied to the symmetric transfer matrix $\mathbf{Z}(j\omega)$. Due to the symmetry of $\mathbf{Z}(j\omega)$, the input directions of the rotation matrix $\mathbf{W}$, associated to the maximum and minimum singular values at $\omega_o = 2\pi 50$ rad/s, are:

$$\overline{w} = \begin{bmatrix} \overline{w}^+ \\ \overline{w}^- \end{bmatrix} = \begin{bmatrix} -\sqrt{2}/2 \\ -\sqrt{2}/2 \end{bmatrix}, \quad \underline{w} = \begin{bmatrix} \underline{w}^+ \\ \underline{w}^- \end{bmatrix} = \begin{bmatrix} \sqrt{2}/2 \\ -\sqrt{2}/2 \end{bmatrix}. \tag{34}$$

Equation (34) gives the conditions under which the input current vector excites the maximum and minimum system gains at the fundamental frequency. The maximum gain is obtained when the components of the input vector are equal, $\overline{w}^+ = \overline{w}^-$, while the minimum gain is obtained when the components are opposite in sign, $\underline{w}^+ = -\underline{w}^-$. The following conditions apply to the magnitude and the phase of the GFL positive and negative sequence currents at ω_o:

$$\begin{aligned} &\text{for } \overline{\sigma}(\omega_o) \text{ then } (|\boldsymbol{i}^+| = |\boldsymbol{i}^-|) \wedge (\angle\boldsymbol{i}^+ = \angle\boldsymbol{i}^-) \\ &\text{for } \underline{\sigma}(\omega_o) \text{ then } (|\boldsymbol{i}^+| = |\boldsymbol{i}^-|) \wedge (\angle\boldsymbol{i}^+ = \angle\boldsymbol{i}^- + \pi). \end{aligned} \tag{35}$$

The singular values of the impedance matrix $\mathbf{Z_N}$ and $\mathbf{Z_P}$, based on the system parameters given in Table I, are shown in Fig. 7(a). In short, it can be seen that as the input current vector is varied in any direction, the system gain will always remain within the internal region defined by these singular value curves.

The singular value concept can be used to evaluate the accuracy of the P-HIL system. The accuracy between the P-HIL and the NCS impedance can be evaluated by calculating the ratio between the P-HIL and NCS impedance:

$$\mathbf{Z_{error}}(j\omega) = \mathbf{Z_P}(j\omega)\,[\mathbf{Z_N}(j\omega)]^{-1} \tag{36}$$

where $\mathbf{Z_{error}}$ provides the error transfer matrix between the P-HIL and the NCS, when the inverse of $\mathbf{Z_N}$ exists. Based on (36), an ideal P-HIL generates an impedance transfer matrix that behaves like the NCS, with $\mathbf{Z_{error}} = \mathbf{I}$ (identity matrix) and singular values of $\mathbf{Z_{error}}$ equal to 1 (or equal to 0 dB) over the frequencies of interest. However, the P-HIL is not able to correctly reproduce the behaviour of the NCS at any frequency, especially at high frequencies where the effect of the delays is pronounced. This finding is also confirmed in Fig. 7(b), which shows the singular values of the $\mathbf{Z_{error}}$ matrix. $\mathbf{Z_{error}}$ is a (2x2) MIMO transfer matrix with two different singular values that can be evaluated at any given frequency. At the fundamental frequency, the maximum and minimum gain values are $\overline{\sigma}_{err}(j2\pi 50)$ = 4 dB and $\underline{\sigma}_{err}(j2\pi 50)$ = 2.2 dB respectively. They represent the gain error between the P-HIL and the NCS impedance at 50 Hz. The aim of an accurate P-HIL is to achieve zero gain error, however both singular

TABLE I
OVERALL SYSTEM PARAMETERS

Parameters	Value
Converter Rated Apparent Power (S_{rated})	5 kVA
DC-Link Voltage (v_{LVDC})	700 V
Nominal Grid Voltage in RMS (v_s)	220 V
Nominal Angular Grid Frequency (ω_o)	$2\pi 50$ rad/s
Switching and Sampling Frequency (f_{sw})	10 kHz
Inductive Filter (L_f)	5 mH
Transformer Leakage Inductance (L_g)	0.5 mH
Capacitive Filter (R_d, C_f)	(10 Ω, 1.5 μF)
PA Output Impedance (R_{pa},L_{pa})	(0.01 Ω, 2.4 mH)
RTDS Time-Step (T_{RT})	50 μs
Low-Pass Filter Bandwidth (ω_c)	$2\pi(450)$ rad/s
Short Circuit Ratio (SCR)	16
X/R Ratio	10
Grid Impedance (R_S, L_S)	(0.25 Ω, 8 mH)
Dip Parameter ($\vec{D}$)	0.5 ∠0

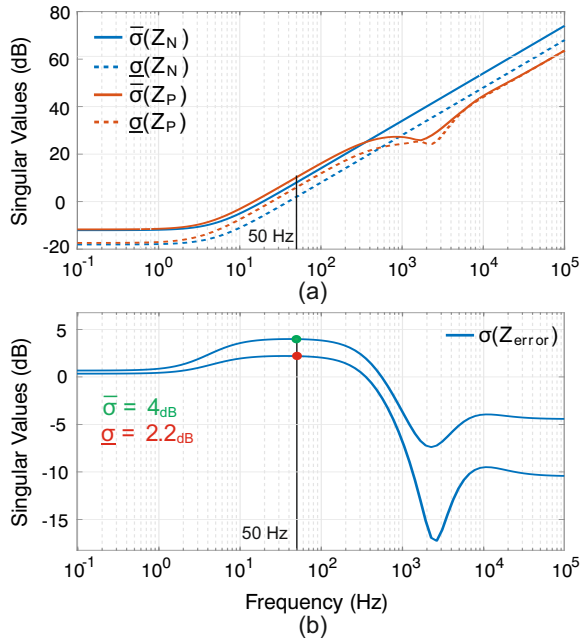

Fig. 7. Singular values plots: (a) $\mathbf{Z_N}$ and $\mathbf{Z_P}$, (b) $\mathbf{Z_{error}}$ under a line-to-line fault with $\vec{D} = 0.5\ \angle 0$, $Z_{PA} \neq 0$ and 450 Hz LPF bandwidth.

values show gain error even at the fundamental frequency. The required P-HIL accuracy depends on the frequency range of the power system phenomena being investigated. For instance, if the analysis is performed under steady-state conditions, the P-HIL must perfectly reproduce the NCS at least at the grid frequency. To test grid-connected converters in a short-circuit scenario, the frequencies below 1 kHz must be accurately represented [12]. Therefore, the ITM-based P-HIL lacks in terms of reliability of the test results.

D. Simulation Results of Line-to-Line Grid Faults in P-HIL

Simulation analyses were performed to validate the singular values of the $\mathbf{Z_{error}}$ transfer matrix. A line-to-line grid fault is simulated in both the NCS and in the DRTS of the P-HIL by setting the fault-side impedance Z_F to be equal to the grid impedance Z_S, ($Z_S = Z_F$), resulting in a positive sequence voltage of 0.75 per unit (p.u.) and a negative sequence voltage of 0.25 p.u. at the PCC. In the following analysis, the GFL converter is connected to the faulty grid while the source voltage is assumed to be zero, $v_s = 0$. The GFL converter injects both positive and negative sequence current components such that they are identical in magnitude but shifted in phase by π, ($\boldsymbol{i}^+ = -\boldsymbol{i}^-$). Figure 8 shows the positive and negative sequence voltages at the PCC in both P-HIL and NCS. The amplitude of the positive and negative sequence voltages in the P-HIL is higher than in the NCS, showing a gain error of 4 dB in both cases, which is also the maximum singular value gain of $\mathbf{Z_{error}}$ at 50 Hz. $\mathbf{Z_{error}}$ therefore provides the maximum singular value when the input current vector components are of equal magnitude and π-shifted in phase.

In a second test, the positive and negative sequence current components injected by the GFL converter have equal magnitude and initial phase, ($\boldsymbol{i}^+ = \boldsymbol{i}^-$). Figure 9 shows the positive

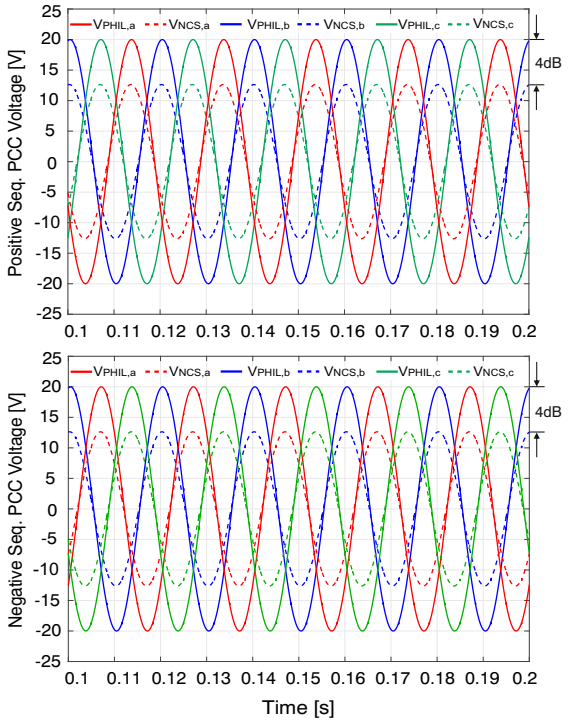

Fig. 8. P-HIL and NCS voltages at the PCC when $v_s = 0$, $\boldsymbol{i}^+ = -\boldsymbol{i}^-$ and $|\boldsymbol{i}^+| = |\boldsymbol{i}^-| = 10$ A, under a line-to-line fault with $\vec{D} = 0.5\ \angle 0$.

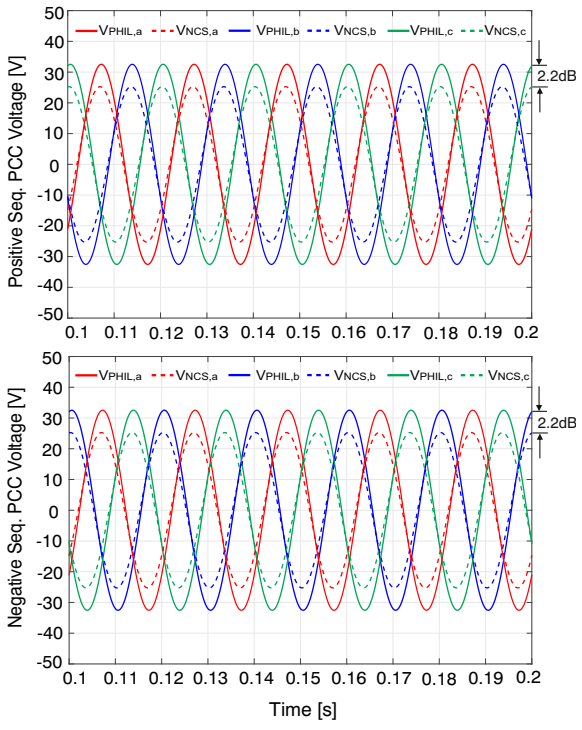

Fig. 9. P-HIL and NCS voltages at the PCC when $v_s = 0$, $\boldsymbol{i}^+ = \boldsymbol{i}^-$ and $|\boldsymbol{i}^+| = |\boldsymbol{i}^-| = 10$ A, under a line-to-line fault with $\vec{D} = 0.5\ \angle 0$.

and negative sequence voltages at the PCC, whereas the gain error between P-HIL and NCS voltages is 2.2 dB, which is the lowest singular value of $\mathbf{Z_{error}}$. It has therefore been confirmed that $\mathbf{Z_{error}}$ provides the minimum singular value when the input vector components are of the same magnitude

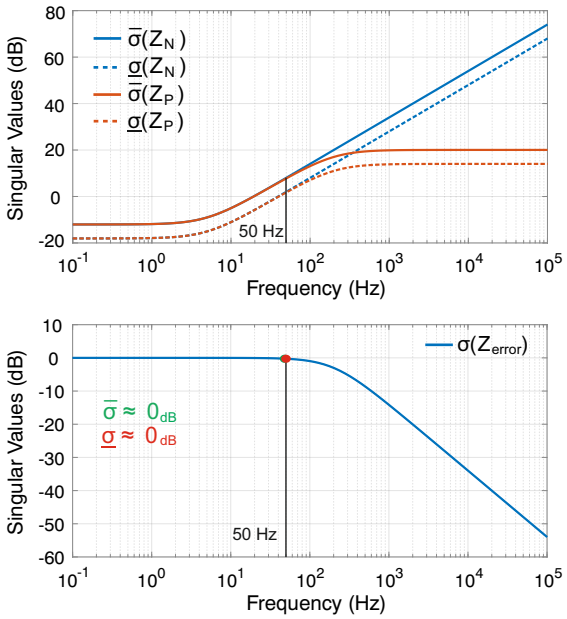

Fig. 10. Singular values plots: (top) $\mathbf{Z_N}$ and $\mathbf{Z_P}$, (bottom) $\mathbf{Z_{error}}$ under a line-to-line fault with $\vec{D} = 0.5\ \angle 0$, $Z_{PA} = 0$ and 200 Hz LPF bandwidth.

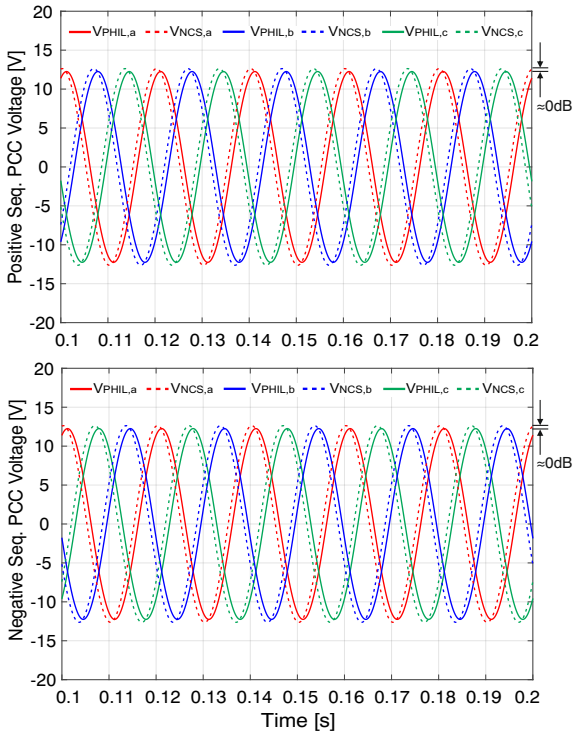

Fig. 11. P-HIL and NCS voltages at the PCC when $v_s = 0$, $\boldsymbol{i}^+ = -\boldsymbol{i}^-$, $|\boldsymbol{i}^+| = |\boldsymbol{i}^-| = 10$ A, under a line-to-line fault with $\vec{D} = 0.5\ \angle 0$ and $Z_{PA} = 0$.

and phase. These results prove that a different PCC voltage gain is expected from the NCS and the P-HIL when the fault is supported by the same injected current values. In turn, a different amount of reactive power is required to achieve the same voltage recovery under LVRT test conditions, as it will be shown in Section V-A.

E. Accuracy Analysis of Line-to-Line Grid Faults in P-HIL Under Ideal Conditions ($Z_{PA} = 0$)

The low frequency error can be explained as a side effect of the not negligible output impedance of the PA, Z_{PA}. In fact, in an ideal scenario with Z_{PA} = 0, the singular values of the matrix $\mathbf{Z_P}$ would be reshaped at low frequency, as shown in Fig. 10. Here, it is shown an increased the accuracy in the very low-frequency range and up to 100 Hz, at the expense of an increasing error in the high-frequency range. This error is the result of a more selective LPF bandwidth ($\omega_c = 2\pi 200$ rad/s) needed to stabilise the P-HIL when Z_{PA} = 0. The LPF removes the high-frequency dynamics of the fault from the model, resulting in different transient behaviour between the P-HIL and the NCS after the fault is applied. At the fundamental frequency, the magnitude error is close to 0 dB, indicating high P-HIL accuracy in steady-state conditions. This analysis is also confirmed by simulations as shown in Figs. 11-12. A time-shift between the P-HIL and the NCS voltages can be seen due to the non-negligible LPF effects on the phase of the fault impedance already at the fundamental frequency.

The transient behaviour of the PCC voltage in the real ($Z_{PA} \neq 0$) and ideal case (Z_{PA} = 0), when a line-to-line fault is applied to both the P-HIL and the NCS, is then analysed. At $t = 0.15s$ a line-to-line fault, with $\vec{D} = 0.5\ \angle 0$, is applied between phase-b and phase-c, while P^* = 0 kW and Q^*= 2 kVAR are kept constant before and after the fault. The results of the comparison between the P-HIL and the NCS

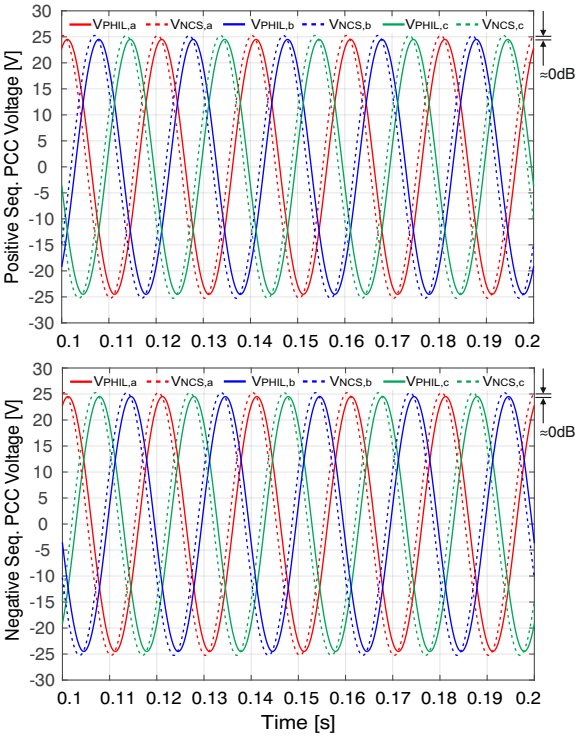

Fig. 12. P-HIL and NCS voltages at the PCC when $v_s = 0$, $\boldsymbol{i}^+ = \boldsymbol{i}^-$, $|\boldsymbol{i}^+| = |\boldsymbol{i}^-| = 10$ A, under a line-to-line fault with $\vec{D} = 0.5\ \angle 0$ and $Z_{PA} = 0$.

in the real and ideal case are shown in Fig. 13 and Fig. 14 respectively. The P-HIL shows a good match with the transient

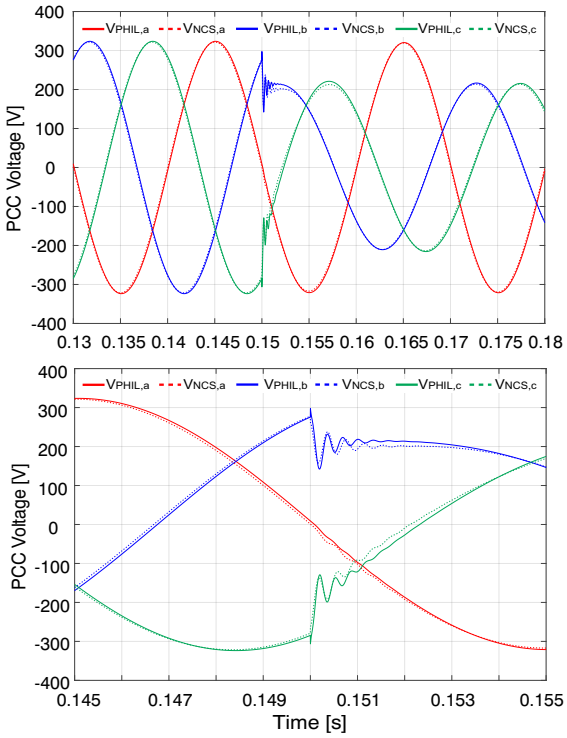

Fig. 13. PCC voltages transient behaviour in P-HIL and NCS under a line-to-line fault with $\vec{D} = 0.5\ \angle 0$, $Z_{PA} \neq 0$, P^* = 0 kW and Q^*= 2 kVAR.

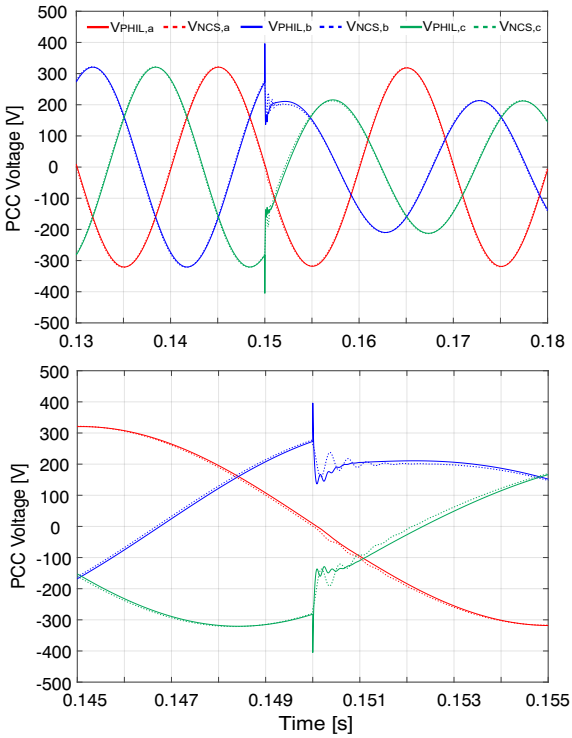

Fig. 14. PCC voltages transient behaviour in P-HIL and NCS under a line-to-line fault with $\vec{D} = 0.5\ \angle 0$, $Z_{PA} = 0$, P^* = 0 kW and Q^*= 2 kVAR.

behaviour of the NCS when $Z_{PA} \neq 0$. This is due to the ability of the output filter impedance Z_{PA} to better emulate the model of the grid impedance at high-frequencies, as also confirmed by the singular values plots in Fig. 7. Instead, when $Z_{PA} = 0$, the transient behaviour of the P-HIL shows high inrush voltages at the PCC, which can be dangerous for the safety of the hardware components. After the inrush point, the high-frequency dynamics are attenuated by the action of the LPF which is designed with a bandwidth of 200 Hz for stability reasons (240 Hz is the critical frequency in this case).

IV. P-HIL Stability Analysis in Asymmetrical Grid Faults

The control structure of a three-phase grid-connected voltage source converter (VSC) in stationary $\alpha\beta$-frame, operating under unbalanced grid condition, is shown in Fig. 15. The voltage across the capacitor of the LCL, $\boldsymbol{v}_{Cf}$, is measured and sent to the dual second-order generalized integrator frequency-locked loop (DSOGI-FLL) for grid synchronization purpose and for extracting the positive-negative sequence components in the grid voltage [23]. An average active-reactive control (AARC) generates the necessary current reference in $\alpha\beta$-frame to cancel out the second-order oscillation in the output active or reactive power, under specific reference conditions. As an example, if only reactive power is injected into the grid by using AARC, P^* = 0 kW and $Q^* \neq 0$ kVAR, the residual instantaneous active power delivered to the grid is zero and without oscillations [21]. The AARC current references, in $\alpha\beta$-frame, are calculated as follows:

$$\boldsymbol{i}^* = \frac{\boldsymbol{v}_{Cf} P^* + \boldsymbol{v}_{Cf}^{\perp} Q^*}{|\boldsymbol{v}_{Cf}^{+}|^2 + |\boldsymbol{v}_{Cf}^{-}|^2} \tag{37}$$

where $\boldsymbol{v}_{Cf}^{\perp}$ is an orthogonal (90° leading) version of the measured voltage vector $\boldsymbol{v}_{Cf}$, while $|\boldsymbol{v}_{Cf}^{+}|$ and $|\boldsymbol{v}_{Cf}^{-}|$ are the amplitudes of the positive and negative sequence components of $\boldsymbol{v}_{Cf}$, respectively. Proportional-resonant (PR) controllers in $\alpha\beta$-frame are used to track sinusoidal current references composed of positive and negative sequence components without steady-state error and without any additional reference frame transformation, closing the current control loop [24].

The PR current controller is expressed as:

$$G_{cc}(s) = K_{p,cc} + K_{r,cc} \frac{s}{s^2 + \omega_0^2} \tag{38}$$

where $K_{p,cc}$ and $K_{r,cc}$ are the proportional and resonant gain of the current controller respectively, while ω_0 is the nominal grid angular frequency. $G_{PWM}(s)$ is the transfer function obtained by combining the computational and the pulse width modulation (PWM) delays:

$$G_{PWM}(s) = \frac{1}{1.5 T_s s + 1} \tag{39}$$

where T_s is the converter sampling time. $G_f(s)$ is the open-loop admittance of the LCL filter from the converter side to the grid side, and it is expressed as:

$$G_f(s) = \frac{i(s)}{v_{PWM}(s)} = \frac{Z_{Cf}}{Z_{Lf} Z_{Lg} + Z_{Lf} Z_{Cf} + Z_{Lg} Z_{Cf}} \tag{40}$$

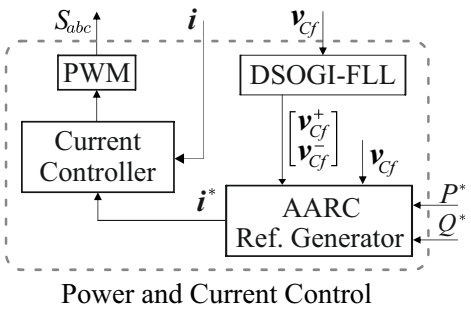

Fig. 15. AARC power and current control structure of a GFL converter under unbalanced grid conditions.

where Z_{Lf}, Z_{Cf} and Z_{Lg} are the impedance of the inductive and capacitive components of the LCL filter, including a damping resistance R_d in series to the capacitor C_f.

A. Converter Output Admittance Model

The admittance model of the whole power converter system can be deduced in its general formulation by paralleling the output admittance of the VSC with the admittance of the synchronization unit [20].

In this paper, the effects of the synchronization unit on the overall output admittance, and consequently on the stability of the P-HIL, are neglected. In fact, the DSOGI-FLL contributes to the overall admittance only at low frequencies (around the nominal frequency), while P-HIL instabilities appear mainly in high-frequency range since they are related to the effects of delays in the loop. Neglecting the synchronization dynamic allows to decouple the positive and negative sequence output admittance of the converter, resulting in a (2x2) diagonal matrix, $\mathbf{Y_o}$. The output admittance of the VSC in the positive and negative sequence frame can be expressed by considering the current controller $G_{cc}(s)$, the PWM transfer function $G_{PWM}(s)$, and the current filter $G_f(s)$, as

$$\mathbf{Y_o} = \begin{bmatrix} Y_o & 0 \\ 0 & Y_o \end{bmatrix}, \; Y_o(s) = \frac{G_f\left(1+\frac{Z_{Lf}}{Z_{Cf}}\right)}{1+G_{cc}G_{PWM}G_f}. \tag{41}$$

B. Multi-Variable Impedance-Based Stability Analysis

The impedance-based criterion in [25] is used to determine the stability of grid-connected converters. Assuming the small-signal model of the grid as an ideal voltage source with in series an impedance $Z(s)$, and assuming that the converter can be modelled as a controlled current source with in parallel an output admittance $Y_o(s)$, the inverter will operate stably if the so-called return ratio $L(s) = Z(s)Y_o(s)$ satisfies the Nyquist criterion [25].

In case of MIMO systems, the multi-variable control system theory should be applied for stability assessment. The generalized Nyquist criterion can be used as it provides a sufficient and necessary stability condition and does not suffer from excessive conservatism. The return ratio (or minor loop) $\mathbf{L}(s)$ for the system under analysis can be expressed as follows:

$$\mathbf{L}(s) = \mathbf{Z}(s)\mathbf{Y}_o(s) = \begin{bmatrix} Z^+ & Z^- \\ Z^- & Z^+ \end{bmatrix} \begin{bmatrix} Y_o & 0 \\ 0 & Y_o \end{bmatrix} \tag{42}$$

The eigenvalue loci of the interconnected system, $\lambda_i(\mathbf{L}(s))$, can be calculated as the eigenvalues of the return ratio $\mathbf{L}(s)$ by imposing the following condition, $det[\lambda\mathbf{I}-\mathbf{L}(s)] = 0$.

$$\begin{aligned} \lambda_1(\mathbf{L}(s)) &= (Z^+ + Z^-)Y_o \\ \lambda_2(\mathbf{L}(s)) &= (Z^+ - Z^-)Y_o \end{aligned} \tag{43}$$

From (43) it results that the system has two eigenvalues, and for the generalized Nyquist criterion, if the minor loop gain $\mathbf{L}(s)$ has no right-half plane poles, then the closed-loop system is stable if both the Nyquist loci of $\lambda_1(\mathbf{L}(s))$ and $\lambda_2(\mathbf{L}(s))$ do not encircle the point $(-1, j0)$.

C. Application of the GNC to the System Under Study

In the following, the GNC presented in the previous section is adopted to assess the stability of an ITM-based P-HIL without and with LPF, $G_{LPF}(s)$, for the system under study (see parameters in Table I).

As first step, it has been verified (but not here reported) that the return ratio $\mathbf{L}(s)$ has no right-half plane poles in none of the cases under study. Then, Fig. 16 plots the eigenvalues of the return ratio for an ITM-based P-HIL, when none LPF filter is applied to the measured currents. Both the eigenvalues encircle the critical point $(-1, j0)$, indicating an unstable interconnected system. A similar analysis is performed for an LPF based ITM with a bandwidth of 450 Hz. The return ratio eigenvalues are plotted in Fig. 17, and none of them encircle the critical point $(-1, j0)$, indicating a stable interconnected system. The filter bandwidth design is based on a compromise between accuracy and stability. The higher is the LPF bandwidth, the more accurate is the P-HIL at high frequencies, however the closer is the system to the instability, and vice versa.

Based on the system parameters given in Table I, an LPF bandwidth of $\omega_c = 2\pi(450)$ rad/s is selected. The phase margins (PMs) of the interconnected system are calculated at the crossing frequency between the converter output impedance, $Z_o = 1/Y_o$, and the eigenvalues of the fault matrix impedance $\mathbf{Z}$(s), which are $\lambda_1(\mathbf{Z}(s)) = (Z^+ + Z^-)$ and $\lambda_2(\mathbf{Z}(s)) = (Z^+ - Z^-)$. With the selected LPF design, the system presents two minimum PMs, $PM_1 = 20°$ and $PM_2 = 28°$ (one for

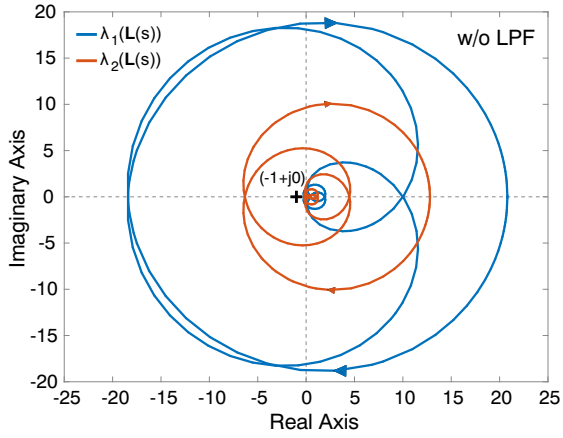

Fig. 16. Nyquist plot of $\lambda_1(\mathbf{L}(s))$ and $\lambda_2(\mathbf{L}(s))$ in ITM w/o LPF.

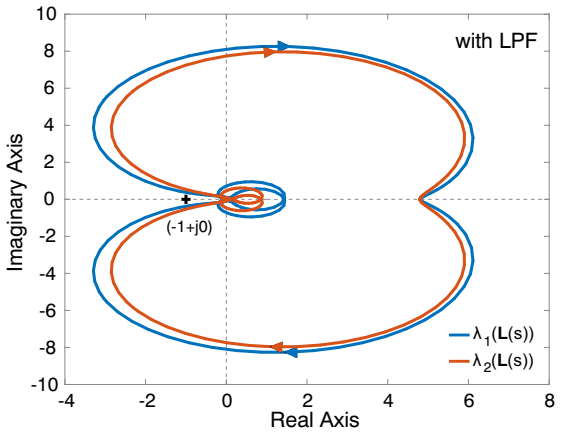

Fig. 17. Nyquist plot of $\lambda_1(\mathbf{L}(s))$ and $\lambda_2(\mathbf{L}(s))$ in ITM with 450 Hz LPF.

each eigenvalue), as shown in Fig. 18. In general, the smallest PM is also the most critical for the stability. For the specific system under analysis, the smallest PM is the one associated to the eigenvalue $\lambda_1(\mathbf{Z}(s))$, and it is calculated at the crossing frequency of 3.52 kHz ($PM_1 = 20°$). This frequency is crucial for a correct stability assessment as it provides detailed information about the frequency range where critically damped oscillations are expected in the real system. Moreover, it provides insights into the frequency response nature of not modelled dynamics and/or parametric uncertainties that may affect the system stability.

D. Effects of the Sampling Time on the P-HIL Stability

With regard to the specific system under investigation, the P-HIL delays strongly affect the phase of the closed-loop system at high-frequencies. As a consequence, uncertainties in the estimated loop delays can lead to a misjudgment of the stability margin and, consequently, the stability of the real system. These findings were verified by a robust stability analysis against the effects of an increasing sampling time. Figure 19 shows the impedance-based stability analysis of the investigated system as the sampling time increases from T_{RT} = 50 μs to T_{RT} = 150 μs. The resulting fault impedance shows a significant deviation in the phase around 3.1 kHz with respect to the previous case in Fig. 18. This deviation results in a reduced stability margin of the whole system, as confirmed by the critical phase margin $PM_1 = 0°$ associated with the eigenvalue $\lambda_1(\mathbf{Z}(s))$. Under this marginally stable condition, a stabilising action would require a reduction of the LPF bandwidth.

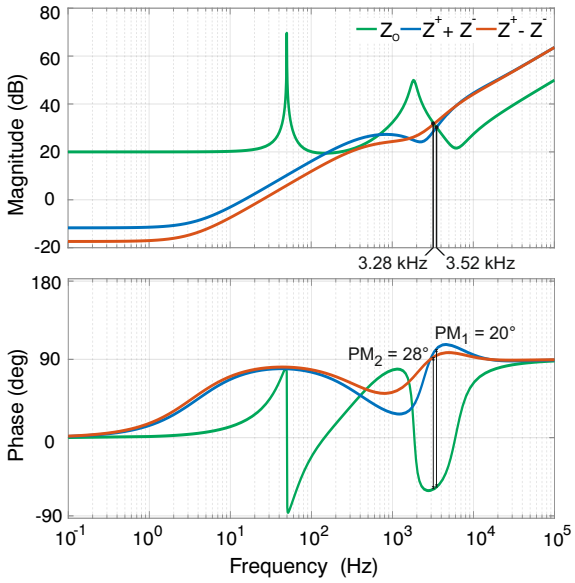

Fig. 18. Impedance-based stability analysis of a P-HIL for GFL converter testing under line-to-line fault, in ITM with 450 Hz LPF bandwidth and a time step of T_{RT} = 50 μs.

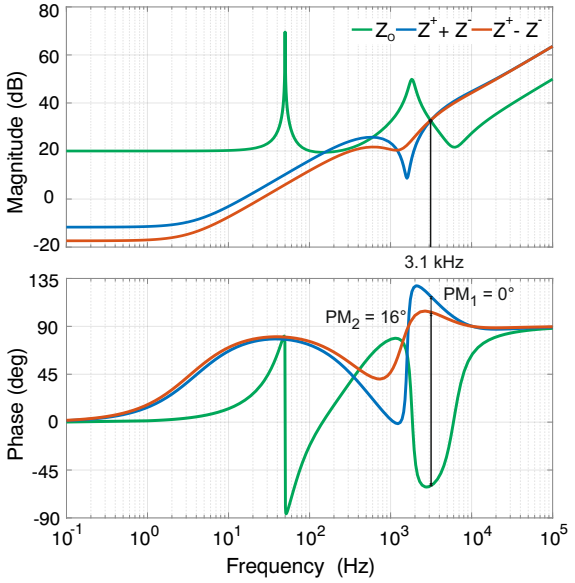

Fig. 19. Impedance-based stability analysis of a P-HIL for GFL converter testing under line-to-line fault, in ITM with 450 Hz LPF bandwidth and a time step of T_{RT} = 150 μs.

E. Necessary Conditions for P-HIL Transient Stability

According to recent German grid codes [1]–[3], dual-sequence current injection is required by the power converter during asymmetrical faults. Under grid faults and weak-grid conditions, converter instability may occur as the synchronization unit is unable to remain synchronized with the voltage at the point of connection. This transient instability phenomenon is called loss of synchronization [26]. A static model identifying the necessary conditions for synchronization stability during asymmetrical grid faults was presented in [26]. Here, it was recognized that the instability occurs as a power transfer problem in an RL-circuit between the converter and the faulted bus. The necessary conditions for the transient stability are given in two-sequence reference frames that are coupled to each other at the fault point. In steady-state condition, when the synchronization is perfectly achieved in the dq^+-positive and dq^--negative rotating reference frame, $v_q^+ = v_q^- = 0$. The necessary conditions for a stable synchronization after a fault

disturbance are the following:

$$I^{+} \leq \frac{|\vec{D}^{+}V_s|}{|Z_{L_g} sin(\phi^{+}_{L_g} + \theta^{+}_{I})|}$$
$$I^{-} \leq \frac{|\vec{D}^{-}V_s|}{|Z_{L_g} sin(\phi^{-}_{L_g} + \theta^{-}_{I})|} \quad (44)$$

where Z_{L_g} and $\phi^{\pm}_{L_g}$ are the magnitude and phase impedance of the three-phase transformer used to isolate the converter from the grid, respectively. $I^{\pm}$ and $\theta^{\pm}_{I}$ are the magnitude and phase of the injected positive and negative sequence currents, respectively. $|\vec{D}^{+}V_s|$ and $|\vec{D}^{-}V_s|$ define the severity of the voltage sag at 50 Hz, for the positive and negative sequences respectively. Under pure reactive current injection, likewise during LVRT scenario, this condition holds: $\theta^{\pm}_{I} = \pm\frac{\pi}{2}$. In this case, the necessary stability conditions are defined by the voltage magnitude at the PCC and the transformer resistance, R_{L_g}, as follows:

$$I^{+} \leq \frac{|\vec{D}^{+}V_s|}{R_{L_g}}$$
$$I^{-} \leq \frac{|\vec{D}^{-}V_s|}{R_{L_g}}. \quad (45)$$

Equation (45) defines the boundaries for a stable transient operation of the converter under asymmetrical grid fault conditions. This stable operating range may decrease depending on the severity $\vec{D}$, and based on the type of fault (e.g. line-to-line, single-line-to-ground, double-line-to-ground). It is worth to mention that (44) and (45) are valid under the condition that the converter currents have a negligible influence on the voltage sequence components at the fault location. This is not realistic, but it is a good way to test the transient stability limits of the synchronization unit. Under this assumption, the transient stability limits in a P-HIL based LVRT test can be expressed as follows:

$$I^{+} \leq \frac{|G_{d,PA}\vec{D}^{+}V_s|}{R_{L_g}} \approx \frac{|\vec{D}^{+}V_s|}{R_{L_g}}$$
$$I^{-} \leq \frac{|G_{d,PA}\vec{D}^{-}V_s|}{R_{L_g}} \approx \frac{|\vec{D}^{-}V_s|}{R_{L_g}}. \quad (46)$$

The P-HIL transient stability limits can be approximated to those of the NCS since the PA delay is negligible at 50 Hz, where the limit conditions are evaluated instead. In (46), R_{L_g} represents only for the copper losses of the transformer, and it is estimated to be in the order of few $m\Omega$. Consequently, the transient stability limits, in an LVRT test with pure reactive power injection, are large enough to avoid instability due to the loss of synchronization after any fault occurrence, even in case of severe faults. This is confirmed by the simulations on the transient behaviour shown in Fig. 13 and Fig. 14. A smooth transition from a no-fault to a fault condition is achieved under an AARC with pure reactive power injection.

V. Experimental Results

Experimental tests in a laboratory environment have been performed to validate the results of the previous analyses. A picture of the P-HIL facility at the CAU in Kiel is shown in Fig. 20. A Danfoss Series FC-302 converter, with 5 kVA rated power, operating with a switching frequency of 10 kHz and equipped with an LCL output filter, is used as dc/ac converter. The converter is connected to a 4-quadrant linear power amplifier PAS 15000 from Spitzenberger-Spies (total three-phase rated power 45 kVA). The control algorithm of the GFL converter is implemented in a dSPACE DS1202 MicroLabBox. The grid fault is simulated in real-time by means of a Real-Time Digital Simulator (RTDS), where also a DSOGI-FLL structure is implemented to estimate in real-time the amplitude of the positive/negative-sequence components of the voltage and current measured the PCC. According to the German FGW TR3 guidelines for LVRT testing, an SCR = 16 and an X/R ratio = 10 are used in the mentioned P-HIL setup. The overall system parameters are given in Table I.

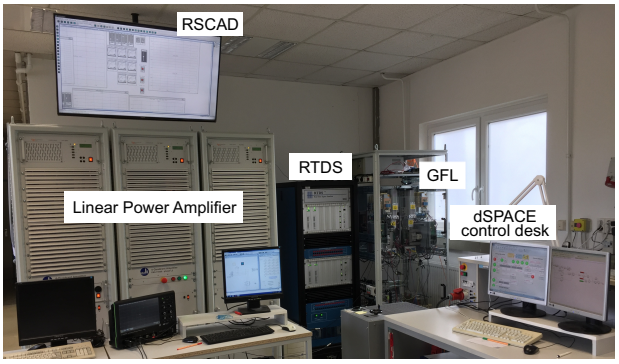

Fig. 20. P-HIL facility at the CAU Kiel.

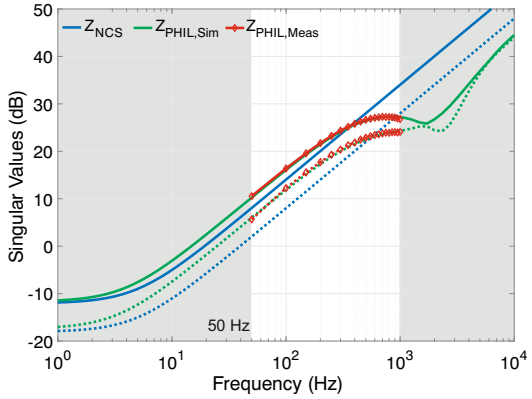

Fig. 21. Experimental P-HIL singular values measurements vs NCS and simulation results in asymmetrical line-to-line grid fault.

A. P-HIL Accuracy Validation in Laboratory

To assess the P-HIL accuracy, the singular values of the emulated grid are derived experimentally. A routine for P-HIL singular values estimation is implemented in the GFL control scheme by injecting the appropriate current vectors to get $\overline{\sigma}_{(i^+,i^-)}$ and $\underline{\sigma}_{(i^+,-i^-)}$, when the source voltage is assumed to be zero, i.e., $v_s = 0$. A mono-frequency perturbing current with adjustable amplitude and frequency is generated at the converter output current range, from 50 Hz to 1 kHz. The magnitude of the three-phase positive/negative sequence of

the voltages and currents at the PCC are measured for each frequency in the RTDS side. The singular values are derived as positive (negative) sequence voltages over positive (negative) sequence currents amplitude ratios. The frequency resolution of the implemented method is equal to 50 Hz. Figure 21 shows the results of the singular values measurements from the laboratory P-HIL, and compare them with those of the analytical P-HIL model, $\mathbf{Z_P}$, and those of the NCS, $\mathbf{Z_N}$. It can be observed that the singular values of the real P-HIL match with the analytical one, $\mathbf{Z_P}$, validating the analytical findings. Furthermore, the singular values of both the previous systems show a deviation with respect to the NCS singular values as expected from the frequency domain analysis.

A LVRT testing of the GFL converter has been performed in the laboratory P-HIL system, and the results have been compared with those of the NCS. The GFL converter under test is connected at its PCC to an emulated low-voltage distribution network with the power rating and the grid parameters given in Table I. The AARC has been implemented to generate the current reference of the GFL converter which is physically connected at the power amplifier side of the emulated grid. The converter injects Q_{PHIL}= 3 kVAR and P_{PHIL}= 0 kW at $t = 0.07$s, whereas a line-to-line fault (between phase-b and phase-c) is emulated in the RTDS side, as shown in Fig. 22. The same grid conditions has been replicated in a NCS simulation, while in this case the converter injects Q_{NCS}= 4 kVAR and P_{PHIL}= 0 kW. It can be seen that the voltage at the PCC is equal in both the P-HIL and NCS, moreover the voltage increased of the 7.2% in both the cases. The positive/negative sequence voltages of the P-HIL and NCS have the same behaviour at different reactive power conditions. The P-HIL setup shows an 1 kVAR reduction (about 20% of S_{rated}) in the required reactive power with respect to the NCS, when the same voltage support is provided. This result proves that different findings in LVRT testing can be obtained in P-HIL setups and confirms how P-HIL accuracy is crucial for correct LVRT compliance testing. Finally, the experimental findings prove that the ITM lacks in terms of accuracy and reliability of the results.

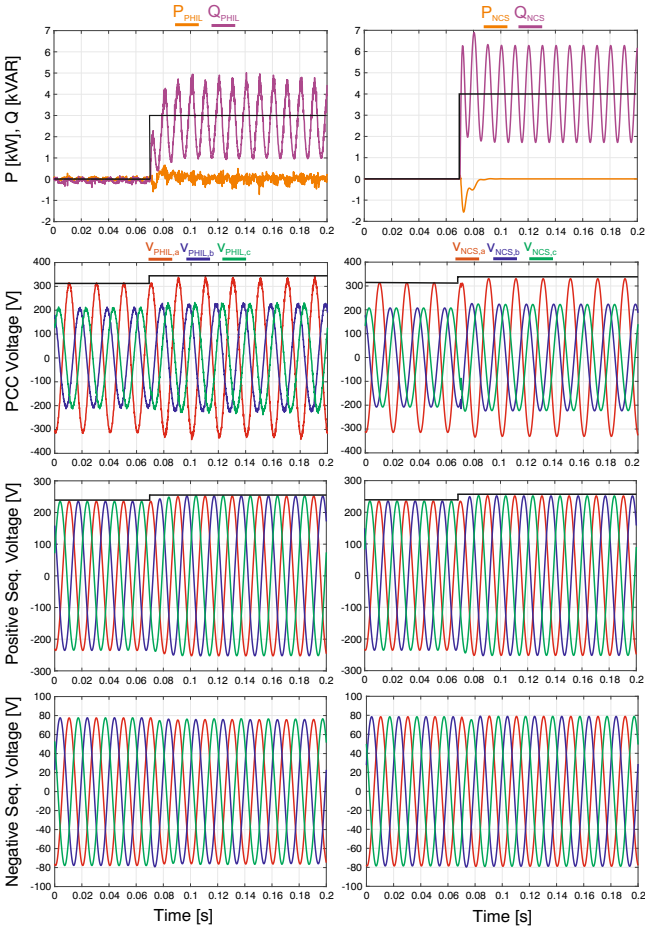

Fig. 22. Laboratory LVRT test of a GFL converter equipped with AARC in P-HIL and NCS under a line-to-line asymmetrical fault with $\vec{D} = 0.5\ \angle 0$.

B. P-HIL Stability Assessment in Laboratory

An assessment of the P-HIL stability boundary in terms of maximum LPF bandwidth of the ITM has been performed in the laboratory, during LVRT testing of GFL converters. Also in this case the AARC has been used to generate the current reference of the GFL convert, while injecting constant Q_{PHIL}= 2 kVAR and P_{PHIL}= 0 kW. To find the stability limits of the system, the LPF bandwidth of the ITM has been increased until critically damped oscillations were observed as result of a 0.3 p.u. step variation in the main voltage supply, v_s. From experiments, critical oscillations with a period of 280 μs were observed and shown in Fig. 23, when a LPF bandwidth of $\omega_c = 2\pi(550)$ rad/s is used. From the stability point of view, the period of the oscillations confirms that critical PMs are expected at frequencies around 3.57 kHz, when the LPF bandwidth is increased above the designed value.

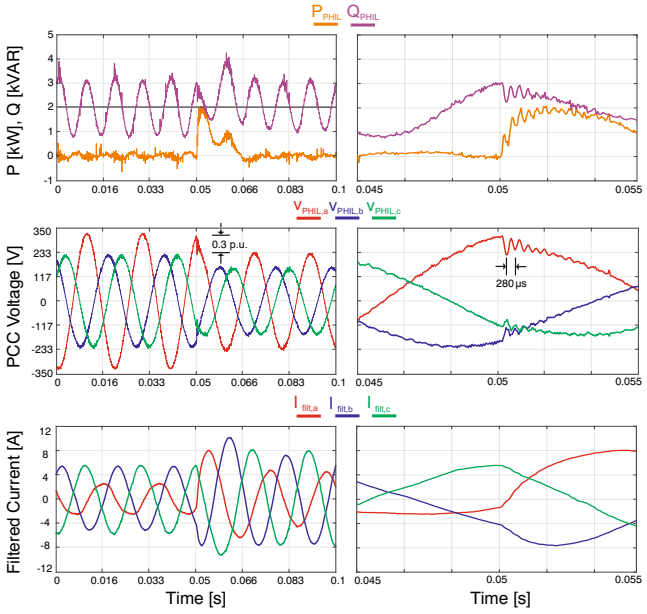

Fig. 23. P-HIL stability test of a GFL converter equipped with AARC under a line-to-line asymmetrical fault with $\vec{D} = 0.5\ \angle 0$, ITM LPF bandwidth of $\omega_c = 2\pi(550)$ rad/s and 0.3 p.u. voltage source variation.

VI. Conclusion

This paper gives the guideline to model asymmetrical grid faults with the aim of assessing P-HIL accuracy and stability in LVRT converter testing. The concept of singular values of MIMO systems is proposed to derive the P-HIL dynamic response in the frequency domain and study the P-HIL accuracy under line-to-line asymmetrical faults. Moreover, the stability of the overall P-HIL system, consisting of a GFL converter connected to a faulty and asymmetrical grid, is studied using the generalized Nyquist criteria for MIMO systems. LVRT testing of a GFL converter in a real P-HIL setup has shown a 20% reduction (% of S_{rated}) in the required reactive power with respect to the NCS, when the same voltage support is provided. Analytical and experimental findings prove that ITM-based P-HIL lacks in terms of reliability of the test results, and more investigation is needed to find the best interface algorithm for LVRT testing of grid converters. Finally, a P-HIL stability test, carried out by setting a marginally stable ITM LPF bandwidth, proved the analytical findings by showing same critically damped oscillations at high frequencies ($\approx$ 3.6 kHz) as expected by the impedance-based stability analysis. This result confirms that the P-HIL delays, and their interaction with the LCL filter of the converter under test, strongly affect the stability of the overall P-HIL system.

References

[1] "Grid integration of generator plants low-voltage – test requirements for generator units to be connected to and operated in parallel with low-voltage distribution networks," DKE- Deutsche Kommission Elektrotechnik Elektronik Informationstechnik in DIN und VDE, Tech. Rep. DIN VDE V 0124-100, Jun. 2020.

[2] "Technical requirements for the connection and operation of customer installations to the medium voltage network (TAR medium voltage)," VDE - Verband der Elektrotechnik Elektronik Informationstechnik e.V., Tech. Rep. VDE-AR-N 4110, Feb. 2017.

[3] "Determination of the electrical characteristics of power generating units and systems, storage systems as well as for their components in medium, high and extra-high voltage grids," FGW e.V. - Fördergesellschaft Windenergie und andere Dezentrale Energien, Tech. Rep. FGW TR3 Rev. 25, Sep. 2019.

[4] A. Frehn, R. Grune, H. Röttgers, and A. Monti, "Influence of the grid parameters during under voltage ride through (UVRT) testing," *Forschung im Ingenieurwesen*, vol. 85, 06 2021.

[5] C. S. Edrington, M. Steurer, J. Langston, T. El-Mezyani, and K. Schoder, "Role of power hardware in the loop in modeling and simulation for experimentation in power and energy systems," *Proceedings of the IEEE*, vol. 103, no. 12, pp. 2401–2409, 2015.

[6] P. C. Kotsampopoulos, F. Lehfuss, G. F. Lauss, B. Bletterie, and N. D. Hatziargyriou, "The limitations of digital simulation and the advantages of phil testing in studying distributed generation provision of ancillary services," *IEEE Transactions on Industrial Electronics*, vol. 62, no. 9, pp. 5502–5515, 2015.

[7] G. F. Lauss, M. O. Faruque, K. Schoder, C. Dufour, A. Viehweider, and J. Langston, "Characteristics and design of power hardware-in-the-loop simulations for electrical power systems," *IEEE Transactions on Industrial Electronics*, vol. 63, no. 1, pp. 406–417, 2016.

[8] A. Benigni, T. Strasser, G. De Carne, M. Liserre, M. Cupelli, and A. Monti, "Real-time simulation-based testing of modern energy systems: A review and discussion," *IEEE Industrial Electronics Magazine*, vol. 14, no. 2, pp. 28–39, 2020.

[9] W. Ren, M. Steurer, and T. L. Baldwin, "Improve the stability and the accuracy of power hardware-in-the-loop simulation by selecting appropriate interface algorithms," *IEEE Transactions on Industry Applications*, vol. 44, no. 4, pp. 1286–1294, 2008.

[10] ——, "An effective method for evaluating the accuracy of power hardware-in-the-loop simulations," *IEEE Transactions on Industry Applications*, vol. 45, no. 4, pp. 1484–1490, 2009.

[11] A. Riccobono, A. Helmedag, A. Berthold, N. R. Averous, R. W. De Doncker, and A. Monti, "Stability and accuracy considerations of power hardware- in-the-loop test benches for wind turbines," *IFAC-PapersOnLine*, vol. 50, no. 1, pp. 10 977–10 984, 2017.

[12] S. Pugliese, M. Liserre, and G. D. Carne, "Enhanced current-type p-hil interface algorithm for smart transformers testing," in *2021 IEEE Energy Conversion Congress and Exposition (ECCE)*, 2021, pp. 1171–1178.

[13] T. Reinikka, H. Alenius, T. Roinila, and T. Messo, "Power hardware-in-the-loop setup for stability studies of grid-connected power converters," in *2018 International Power Electronics Conference (IPEC-Niigata 2018 -ECCE Asia)*, 2018, pp. 1704–1710.

[14] L. M. Tolbert, F. Wang, K. Tomsovic, K. Sun, J. Wang, Y. Ma, and Y. Liu, "Reconfigurable real-time power grid emulator for systems with high penetration of renewables," *IEEE Open Access Journal of Power and Energy*, vol. 7, pp. 489–500, 2020.

[15] R. Uhl and A. Monti, "Validation of the concept for a wideband-frequency grid impedance based grid emulator," in *2020 IEEE 29th International Symposium on Industrial Electronics (ISIE)*, 2020, pp. 1296–1303.

[16] N. Ainsworth, A. Hariri, K. Prabakar, A. Pratt, and M. Baggu, "Modeling and compensation design for a power hardware-in-the-loop simulation of an ac distribution system," in *2016 North American Power Symposium (NAPS)*, 2016, pp. 1–6.

[17] T. S. Ustun, S. Sugahara, M. Suzuki, J. Hashimoto, and K. Otani, "Power hardware in-the-loop testing to analyze fault behavior of smart inverters in distribution networks," *Sustainability*, vol. 12, p. 9365, 11 2020.

[18] A. Mäkinen, T. Messo, and H. Tuusa, "Power hardware in-the-loop laboratory test environment for small scale wind turbine prototype," in *2014 16th European Conference on Power Electronics and Applications*, 2014, pp. 1–10.

[19] M. U. Rafiq, S. Pugliese, and M. Liserre, "Modeling of symmetrical and asymmetrical grid faults for p-hil accuracy analysis in lvrt tests," in *2022 IEEE Energy Conversion Congress and Exposition (ECCE)*, 2022, pp. 1–8.

[20] S. Pugliese, Y. Kwon, and M. Liserre, "Positive-negative sequence srf-pll model for accurate stability analysis in grid-tied converters," in *2020 IEEE Energy Conversion Congress and Exposition (ECCE)*, 2020, pp. 3593–3600.

[21] R. Teodorescu, M. Liserre, and P. Rodriguez, *Grid converters for photovoltaic and wind power systems*. John Wiley & Sons, 2011.

[22] S. Skogestad and I. Postlethwaite, *Multivariable feedback control: analysis and design*. John Wiley & Sons, 2005.

[23] P. Rodríguez, A. Luna, I. Candela, R. Mujal, R. Teodorescu, and F. Blaabjerg, "Multiresonant frequency-locked loop for grid synchronization of power converters under distorted grid conditions," *IEEE Transactions on Industrial Electronics*, vol. 58, no. 1, pp. 127–138, 2011.

[24] S. Pugliese, S. Flacke, Z. Zou, and M. Liserre, "High-frequency harmonic current control of power converters," in *2019 IEEE Energy Conversion Congress and Exposition (ECCE)*, 2019, pp. 6915–6921.

[25] J. Sun, "Impedance-based stability criterion for grid-connected inverters," *IEEE Transactions on Power Electronics*, vol. 26, no. 11, pp. 3075–3078, Nov 2011.

[26] M. G. Taul, S. Golestan, X. Wang, P. Davari, and F. Blaabjerg, "Modeling of converter synchronization stability under grid faults: The general case," *IEEE Journal of Emerging and Selected Topics in Power Electronics*, vol. 10, no. 3, pp. 2790–2804, 2022.

VII. Biography Section

Sante Pugliese (M'18) received the M.Sc. degree in Automation Engineering and the Ph.D. degree in Electrical and Information Engineering from the Politecnico di Bari, Bari, Italy, in 2013 and 2018, respectively. In 2017, he was a Visiting Scholar with the Chair of Power Electronics, Kiel, Germany, where he is currently a Post-Doctoral Researcher. In 2018-2019, he was Post-doc responsible in the EEMSWEA (0325797A) research project, Medium Voltage Grid Analyzer - Mittel Spannungs Netz Analyse. In 2020 he was Post-doc responsible in the Add-On (0350022B) research project funded by the Bundesministerium für Wirtschaft und Energie. His research interests include power converters and control techniques for distributed power generation systems based on renewable energies.

Marco Liserre (S'00-M'02-SM'07-F´13) received the MSc and PhD degree in Electrical Engineering from the Bari Technical University, respectively in 1998 and 2002. He has been Associate Professor at Bari Technical University and from 2012 Professor in reliable power electronics at Aalborg University (Denmark). From 2013 he is Full Professor and he holds the Chair of Power Electronics at Kiel University (Germany). He got offered and declined professorships at several universities. He has published more than 700 technical papers (1/3 of them in international peer-reviewed journals), a book and 5 granted Patents. These works have received more than 50.000 citations. Marco Liserre is listed in ISI Thomson report "The world's most influential scientific minds" from 2014. In 2023 he joined part-time Fraunhofer ISIT as Deputy Director and Director of a new Center for "Electronic Energy Systems" funded for 5 Million Euro.

He is member of IAS, PELS, PES and IES. He has been serving all these societies in different capacities. In PELS he was AdCom member, Co-Editor of the IEEE Open Access Journal in Power Electronics, Associate Editor of TPEL and JESTPE, Guest Editor of Several Special Issues of JESTPE, Technical Committee Chairman of the Committee on Electronic Power Grid Systems and Member of the IEEE Digital Committee, IES-Liaison responsible, eGrid 2021 Workshop Co-chairman and PEDG 2022/PEDG 2023 Co-chairman the first organized in Kiel. He has received 5 IEEE Awards, including the prestigious 2018 IEEE-IES Mittelmann Achievement Award and 6 journal awards.

Muhammad Usman Rafiq received the B.Sc. degree in Electrical Engineering from Air University, Pakistan, in 2018 and the M.Sc. degree in Electrical Engineering and Information Technology from Kiel University, Germany, in 2022. He worked as a research assistant at the Chair of Power Electronics, Kiel, Germany in 2022. After that, he joined the Maschinenfabrik Reinhausen GmbH, Germany, where he is currently working as project engineer on the development of "Industrialisation of the MMC Platform for the STATCOM MMC Application".